Int. J. Electrochem. Sci., 10 **(2015)** 10565 - 10575

International Journal of
ELECTROCHEMICAL
SCIENCE
www.electrochemsci.org

Synthesis and Electrochemical Performance of $Fe_2(MoO_4)_3$/RGO Nanocomposite Cathode Material for Sodium-ion Batteries

VanTu Nguyen, YueLi Liu, Shah Abdul Hakim, Shuang Yang, Amr Rady Radwan, Wen Chen[*]

State Key Laboratory of Advanced Technology for Materials Synthesis and Processing, School of Material Science and Engineering, Wuhan University of Technology, Wuhan 430070, P. R. China
[*]E-mail: chenw@whut.edu.cn

Received: 26 July 2015 / *Accepted:* 22 October 2015 / *Published:* 4 November 2015

$Fe_2(MoO_4)_3$/reduced graphene oxide (RGO) nanocomposite was prepared by precipitation methods and used as high rate cathode for sodium-ion battery. The $Fe_2(MoO_4)_3$/RGO sample has the type monoclinic structure, and the conductivity is increased with the presence of graphene. This sample displays the best electrochemical performance with large capacity, structure stability, high coulombic efficiency and stable cyclic. As the charge/discharge current density at 1.5 C, the initial specific capacity of $Fe_2(MoO_4)_3$/RGO nanocomposite is 80.02 mAh g^{-1}, and remains 75.92 mAh g^{-1} after 50 cycles.

Keywords: NASICON. Iron molybdate. $Fe_2(MoO_4)_3$/RGO. Sodium ion battery. Cathode material

1. INTRODUCTION

Sodium-ion batteries (SIBs) are the most promising alternatives to lithium-ion batteries due to the low cost and abundance of sodium element in the earth. The chemical similarity of sodium ion toward lithium ion enables some electrode materials used in Li-ion batteries (LIBs) to be applied for SIBs. Special for the application in the large-scale energy storage, smart grid and solar/wind energy, and the problem of low-cost would be a big challenge [1-2].

In recent years, many cathode materials for sodium-ion battery have been reported such as Na_xMO_2 [3-7], $Na_3Fe_2(PO_4)_3$ [8], $Na_3V_2(PO_4)_3$ [9-11], Na_2MPO_4F [12-14], $NaFePO_4$ [15, 16], V_2O_5 [17], NASICON compounds [18-22] and organic compounds [23, 24]. NASICON-$Fe_2(MoO_4)_3$ has been shown as a cathode candidate for sodium storage due to the cheap, non-toxic of iron and its open three dimensions framework, however, its poor cycle-ability and low electric conductivity limit its further application [25-27]. However, these studies are still limited by the slow sodium insertion into

$Fe_2(MoO_4)_3$, which derives from the nature of two phase reactions and its low conductivity. In order to overcome these limitations, a better method to design electrodes with change morphologies and nanostructures used in SIBs is proposed. The electrode materials with a variety of nanostructure or nanoarchitecture are appealing to increase the specific energy density and rate capacity due to their large surface area increasing the contact between electrode and electrolyte, short path lengths for both Na^+ ion diffusion and electron transport, improved ionic and electronic conductivity and enhanced mechanical strength and structural integrity represent [28-30].

Graphene is a large monolayer sheet of sp^2 bonded carbon, which has unique optical, electrical, mechanical, and electrochemical properties. The most important chemically derived graphene is graphene oxide (defined as single layer of graphite oxide). Reduced graphene oxide (RGO) has high aspect ratio and good electronic transport properties, which is expected to facilitate the kinetics of electrochemical reactions [31-33]. In some applications, graphene has been used to form composite or hybrids as a highly conductive network in the fields of batteries [34-36]. Recently, electrode materials of sodium ion batteries based on graphene have been reported [13, 37].

In this paper, we applied wet chemistry to synthesis $Fe_2(MoO_4)_3$/RGO nanocomposite. The field emission scanning electrode microscope (FESEM) test shows that the $Fe_2(MoO_4)_3$/RGO nanocomposite formes an interpenetrating network structure. The X-ray diffraction (XRD) and X-ray photoelectron spectroscopy (XPS) analysis confirms that the $Fe_2(MoO_4)_3$ shows monoclinic crystal structure and mixture element states in the nanocomposite. The electrochemical properties of the $Fe_2(MoO_4)_3$/RGO nanocomposite were studies by electrochemical impedance spectroscopy (EIS) and galvanostatic charge-discharge measurement as a cathode material. The results indicate that $Fe_2(MoO_4)_3$/RGO nanocomposite has high specific capacity and good cycling stability act as a cathode material for SIBs. To the best of our knowledge, no reported is available on $Fe_2(MoO_4)_3$/RGO nanocomposite and their electrochemical performance as cathode material for sodium-ion batteries.

2. EXPERIMENTAL

2.1. Preparation of $Fe_2(MoO_4)_3$/RGO nanocomposite

Graphene oxide (diameter of 50–100 nm, thickness of 0.8 nm, 80 % single layer ratio, 99 % purity, BET surface area of 500–600 $m^2 g^{-1}$) was purchased from Nanjing XF NANO Co. Ltd.

$Fe_2(MoO_4)_3$/RGO nanocomposite was prepared by a precipitation method. The RGO content is 5, 8, 10 and 12 wt.% in the original synthesis process. The GO was dispersed in water under ultrasonic conditions for 10 hours, until to obtain a homogeneous yellow solution. Then $(NH_4)_6Mo_7O_{24}\cdot 4H_2O$ was dissolved in solution with the GO and acidified by nitric acid, stoichiometric amount of $Fe(NO_3)_3\cdot 9H_2O$ solution was slowly added under continuous stirring with boiling 60 minutes. Then mixture precipitate is dispersed under ultrasonic conditions for 5 hours. Finally precipitate was filtered, washed and calcined at 400- 500 ^oC in a mixture N_2-H_2 with 5 % H_2 (v/v) for 10 hours.

2.2. Characterization

The crystalline structure of the sample was characterized by a powder X-ray diffraction spectrometer (XRD, PertrPro PANalytical, Nertherlands) equipped with Cu Kα radiation (1.5418 Å). The morphology of the sample was observed by the field emission scanning electron microscope (FESEM, JSM-6700F, JEOL, Tokyo, Japan). X-ray photoelectron spectroscopy (XPS) measurements were acquired using a VG Multilab 2000, with Al Kα the as the radiation source. All XPS spectra were corrected by the C_{1s} line at 284.8 eV. The Brunauer-Emmett-Teller (BET) specific surface area of the powders was analyzed in a nitrogen adsorption-desorption apparatus（BET, TriStar II 3020, Micrometrics, American). Raman spectroscope equipped with a 633 nm laser (Raman; model Renishaw Invia, Britain) was employed to get the structural information.

2.3. Electrochemical measurements

The eletrochemical properties were investigated in CR2025 coin type cells with a metal sodium foil as the anode electrode. The electrolyte is 1 M $NaClO_4$ in propylene carbonate (PC). The working electrode was prepared by spreading the slurry of the active materials $Fe_2(MoO_4)_3$/RGO nanocomposite (80 wt.%), acetylene black (15 wt.%), and binder polytetrafluoroethylene (PTFE) (5 wt.%) on Ni gauze. The electrode was dried at 100 ^oC in vacuum for 10 hours prior to use. Polypropylene micro-porous film (Cellgard 2300) is used as a separator. The cells were assembled in an argon-filled glove box at room temperature. For galvanostatic charge-discharge test was carried out on a Land BT2000 battery test system (Wuhan, China) at ambient temperature. The specific capacities in this article were calculated based on the overall mass of the composite. The cyclic voltammetry (CV) and electrochemical impedance spectroscopy (EIS) were measured by Autolab Potentiostat (Potentiostat 30, Metrohm Autolab, Netherlands).

3. RESULTS AND DISCUSSION

3.1. Morphology and structure

X-ray diffraction (XRD) was used to confirm the phase of $Fe_2(MoO_4)_3$ in the as-prepared composites. XRD patterns of the samples are shown on Figure 1(a), it can be indicated that most of the peaks can be well indexed to the reflections of monoclinic structure of $Fe_2(MoO_4)_3$ (JCPDS No. 01-072-0935) and the peak at 26.65^o indicates the existence of the graphite from the reduced graphene oxide [13, 33]. But the diffraction peaks from the RGO do not clearly observe in the pattern due to their weak crystallinity and the overlap of the weak diffraction of the graphite at 2θ of 26.65 degree with that of $Fe_2(MoO_4)_3$. XRD patterns of $Fe_2(MoO_4)_3$/RGO composites were indexed with a monoclinic lattice using the program Jade 6.5. The unit cell lattice parameters of all the experimental $Fe_2(MoO_4)_3$/RGO phases are summarized in Table 1. It can be seen that, after modifying RGO, the lattice parameters changes small with different content of RGO. It is confirmed that the crystal

structure of monoclinic $Fe_2(MoO_4)_3$ is not changed with the presence of RGO, and the refined unit cell lattice parameters of $Fe_2(MoO_4)_3$/RGO nanocomposte is constant.

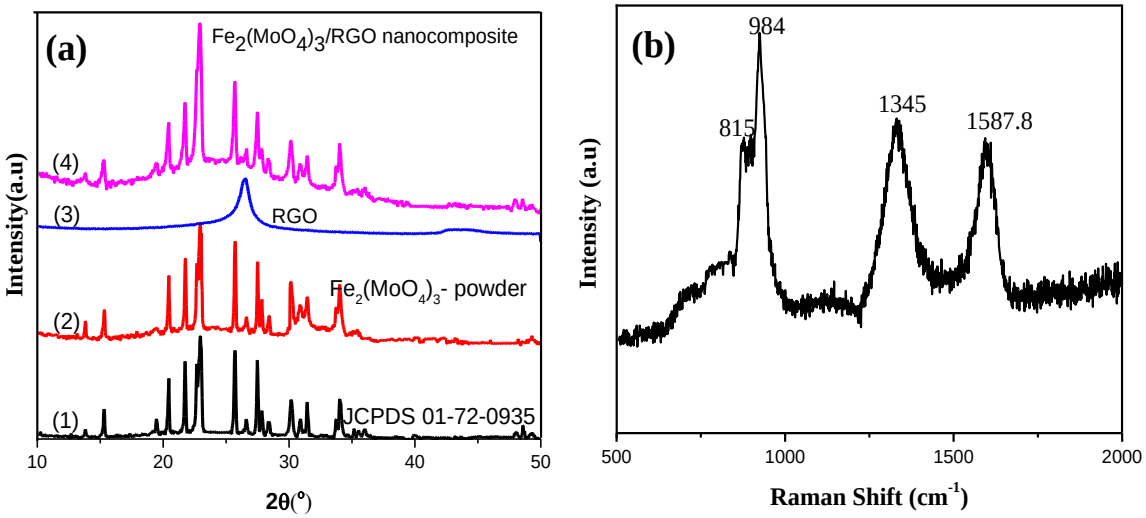

Figure 1. (a) XRD patterns of $Fe_2(MoO_4)_3$ powder and $Fe_2(MoO_4)_3$/RGO nanocomposite (1)-JCPDS 01-72-0935; (2)-$Fe_2(MoO_4)_3$ powder; (3)-RGO; (4)-$Fe_2(MoO_4)_3$/RGO nanocomposite; (b) Raman spectrum of $Fe_2(MoO_4)_3$/RGO nanocomposite.

Table 1. Refined unit cell lattice parameters for $Fe_2(MoO_4)_3$/RGO nanocomposite cells with 0, 5, 8, 10 and 12 wt.% RGO contents.

RGO contents (wt.%)	a(Å)	b (Å)	c (Å)	β (°)	V(Å^3)
0.0	15.72664	9.19676	18.25146	125.5395	2148.04
5	15.72667	9.19678	18.25145	125.5396	2148.10
8	15.72665	9.19677	18.25148	125.5396	2148.05
10	15.72666	9.19679	18.25152	125.5398	2148.12
12	15.72668	9.19678	18.25148	125.5399	2148.11

The structure of the $Fe_2(MoO_4)_3$/RGO nanocomposite is further characterized by Raman spectroscopy. As shown in Fig. 1b, the peaks at 984, 815 refer to M=O stretch (A_g, υ_s), M=O stretch (A_g, υ_{as}), respectively. The peaks at 1587.8 and 1345 cm^{-1} correspond to G band (E_{2g} symmetry, in-plane bond-stretching motion of pairs of sp^2 C atoms) and D band (defect-related) of graphene sheet [38, 39]. The characteristic peaks of $Fe_2(MoO_4)_3$ particles and RGO appear at the same time, suggesting the formation of the $Fe_2(MoO_4)_3$ /RGO nanocomposite.

Figure 2 presents the FESEM images of $Fe_2(MoO_4)_3$/RGO nanocomposite, which the particles are micrometer-sized porous spheres. It can be seen that $Fe_2(MoO_4)_3$ particles and RGO buid a uniform and homogeneous macro-morphology (Figure 2(a)). The Brunauer-Emmett-Teller (BET) specific surface area of $Fe_2(MoO_4)_3$/RGO and $Fe_2(MoO_4)_3$ powder have been estimated to be 21.59 m^2 g^{-1} and 1.63 m^2 g^{-1}, respectively. The $Fe_2(MoO_4)_3$/RGO nanostructure can provide a huge active surface areas

and structure stability, which means a large electrochemical reaction points and reaction stability, as well as high specific capacity and stabe cycle for the electrode of SIBs. Na^+ ions may be easily diffuse into and out of the $Fe_2(MoO_4)_3$/RGO due to their periodic and porous structure at the nanometer scale.

Na^+ ions can easily diffuse into and out of the $Fe_2(MoO_4)_3$/RGO due to their periodic and porous structures at the nanometer scale. The inter-connecting RGO provides fast transport pathways for electron, which provides effective transport between the individual $Fe_2(MoO_4)_3$ particles. Thus, the nanocomposite materials are expected to significantly enhance the batteries performance by improving Na^+ ion and electron transport. Also, the surface roughness of $Fe_2(MoO_4)_3$ nanoparticles provides more interface area between $Fe_2(MoO_4)_3$ and electrolyte.

The formation of $Fe_2(MoO_4)_3$/RGO nanocomposite is further investigated using X- ray photoelectron spectroscopy (XPS). It is well known that the electrochemical properties of the sample is related with their sizes and phases as well as their chemical binding states. The XPS survey spectra in Figure 3(a) show that Fe, Mo, C and O elements coexist. The core level binding energies of C1s spectrum shown in Figure 3(b) can be apparent peaks at 284.7eV and 288.6eV, respectively, which are the characteristic peaks of sp^2 hybridized graphite-like carbon atoms of RGO and in atoms abound to oxygen atoms. Further, the spectra of Fe2p and Mo3d in Figure 3(c) and 3(d) show the characteristic peaks of Fe^{3+} state and Mo^{6+} state located at 711,79 eV and 232.8 eV, respectively. Both samples with and without RGO have the unchanged characteristic peaks of Fe2p and Mo3d (711.79 eV and 232.8 eV), which implies that the presence of RGO does not alter the state of Fe^{3+} and Mo^{6+} in $Fe_2(MoO_4)_3$.

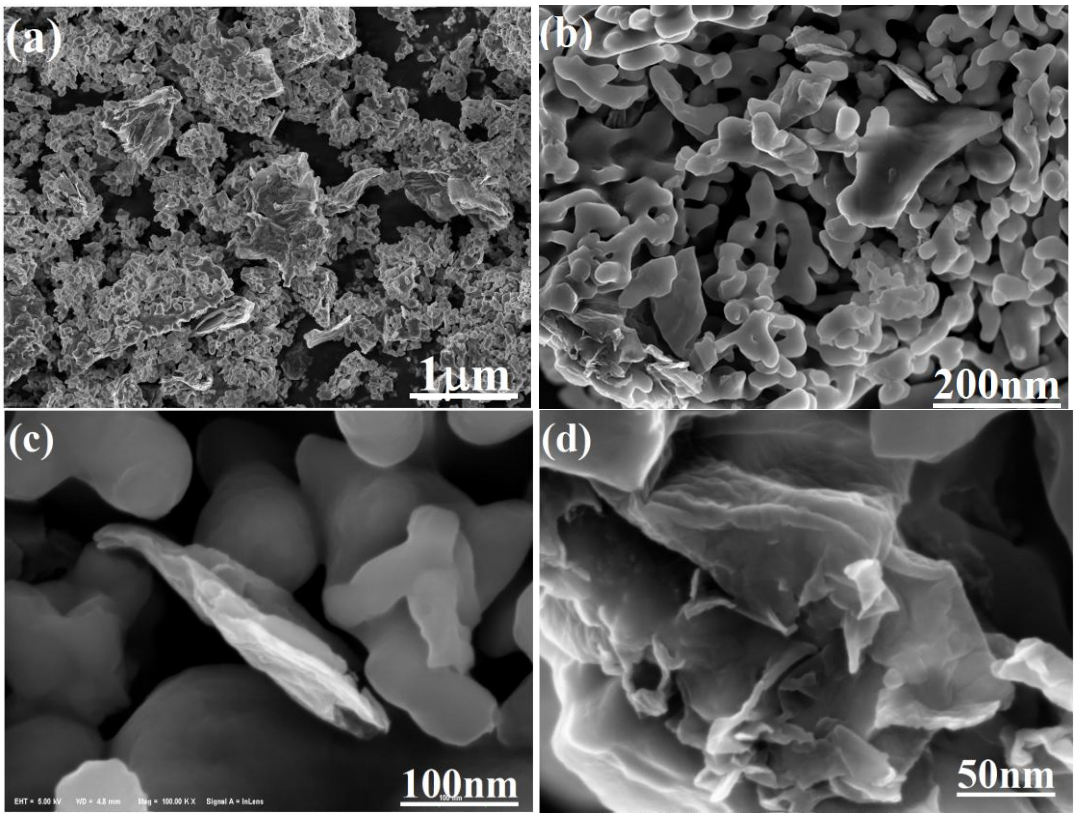

Figure 2. (a) and (b) SEM images of $Fe_2(MoO_4)_3$/RGO nanocomposite; (c) and (d) FESEM images of $Fe_2(MoO_4)_3$/RGO nanocomposite.

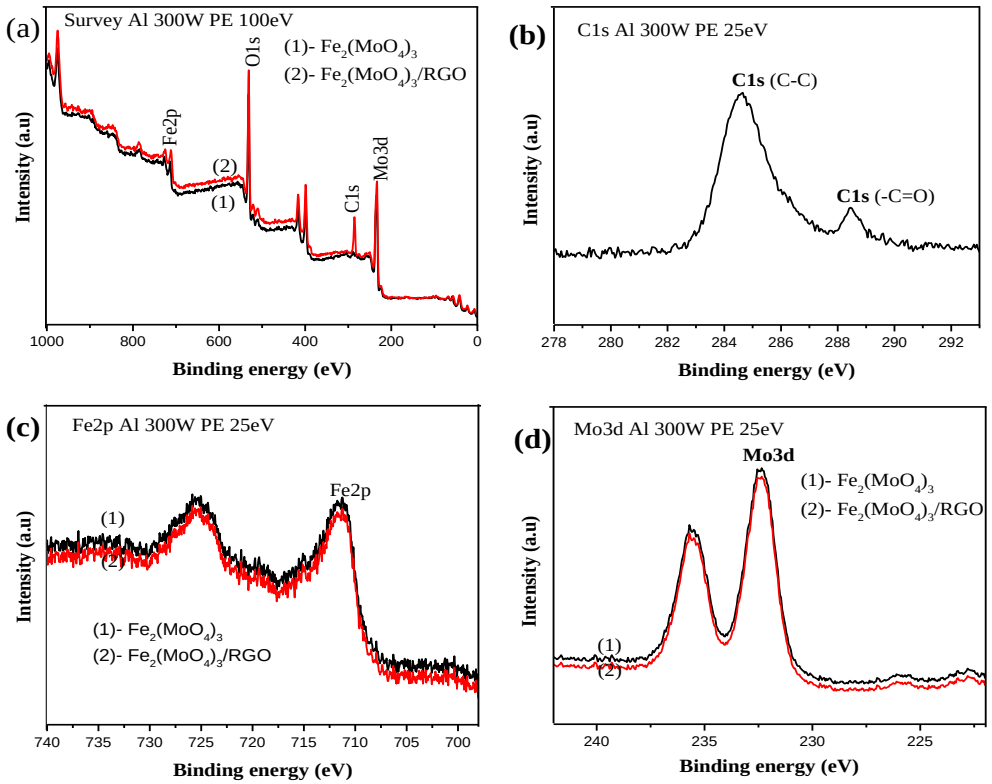

Figure 3. X-ray photoelectron spectra of $Fe_2(MoO_4)_3$ powder and $Fe_2(MoO_4)_3$/RGO nanocomposite. (a) Survey spectra; (b) C1s spectrum; (c) Fe2p spectra, (d) Mo3d spectra.

3.2 Electrochemical performances and rection mechanism

The cyclic voltammetry curves of $Fe_2(MoO_4)_3$/RGO nanocomposite electrode between 1.5 V and 3.5 V at a scanning rate of 0.1 mVs^{-1} are shown in Figure 4(a). Two current peaks of cathode at 2.53 and 2.62 V are observed during the first reduced and transferred to 2.63 V and 2.54 V in the next. In all oxidation, there are two peaks of anode corresponding at 2.57 and 2.72 V. The intensity of the peaks are well maintained in all subsequent cycles. The results are in good agreement with the galvanostatic cycling profiles and indicates two-step mechanism for reversible electrochemical reaction of $Fe_2(MoO_4)_3$ with sodium. And it can be expressed as follows [18].

$$Fe_2(MoO_4)_3 + xNa^+ + xe^- \rightarrow Na_xFe_2(MoO_4)_3 \text{ (the first discharge process, x=1, 2)} \quad (1)$$

$$Na_xFe_2(MoO_4)_3 \leftrightarrow Fe_2(MoO_4)_3 + xNa^+ + xe^- \text{ (discharge/charge process)} \quad (2)$$

On the Fig.4a, the reduction/oxidation betweens $Fe_2(MoO_4)_3$ and $Na_xFe_2(MoO_4)_3$ are shown as follow:

$$\text{At peak (2.57V), anodic process: } Na_2Fe_2(MoO_4)_3 - 1e^- = NaFe_2(MoO4)_3 + Na^+ \quad (3)$$

$$\text{At peak (2.72 V), anodic process: } NaFe_2(MoO_4)_3 - 1e^- = Fe_2(MoO_4)_3 + Na^+ \quad (4)$$

$$\text{At peak (2.62V), cathodic process: } Fe_2(MoO_4)_3 + 1e^- + Na^+ = NaFe_2(MoO_4)_3 \quad (5)$$

$$\text{At peak (2.53 V), cathodic process: } NaFe_2(MoO_4)_3 + 1e^- + Na^+ = Na_2Fe_2(MoO_4)_3 \quad (6)$$

These results clearly reveal that the insertion/extraction of Na^+ ions only occur inside $Fe_2(MoO_4)_3$ rather than on the RGO. RGO function is only used as a conducting material, which does not participate in the redox process.

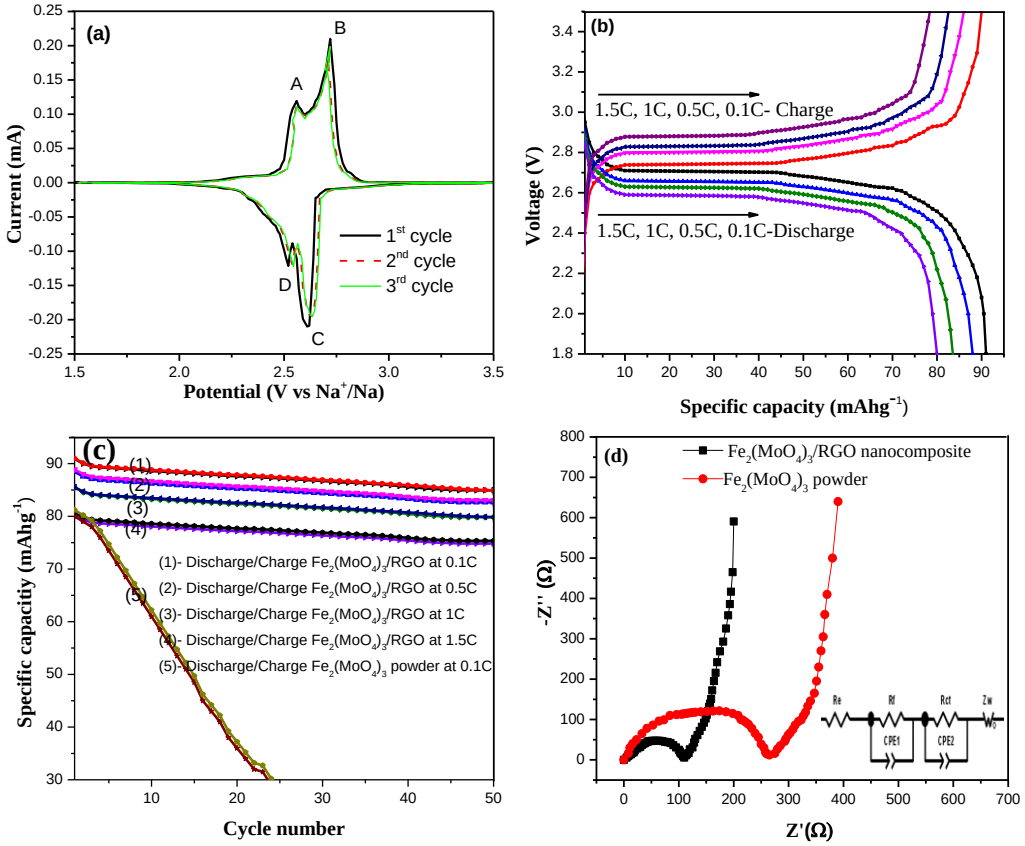

Figure 4. (a) The third cyclic voltammetry curves of $Fe_2(MoO_4)_3$ nanocomposite electrode at a voltage scanning rate of 0.1 mV $s^{-1;}$ (b) Ganvanostatic curves of $Fe_2(MoO_4)_3$/RGO nanocomposite/ Na cell at a current rates of 0.1, 0.5, 1, and 1.5 C; (c) The specific capacities of $Fe_2(MoO_4)_3$/RGO nanocomposite and $Fe_2(MoO_4)_3$ powder at 0.1, 0.5, 1 and 1.5 C (Electrolyte is 1M $NaClO_4$ in propylene cacbonate (PC)); (d) EIS plots of $Fe_2(MoO_4)_3$ powder and $Fe_2(MoO_4)_3$/RGO nanocomposite after 3 cycles at 9 mA g^{-1} in the frenquency range between 100 kHz and 0.1 Hz at open circuit voltage (OCV) with 5 mV amplitude voltage (inset shows the equivalent circuits corresponding to the Nyquist plots). All gravimetric capacity of the $Fe_2(MoO_4)_3$/RGO nanocomposite is calculated based on the total weight of the comosite that contains approximately 10 wt.% RGO.

Figure 4(b) shows the first discharge/charge profiles of $Fe_2(MoO_4)_3$/RGO nanocomposite/Na cells at a rate of 0.1, 0.5, 1 and 1.5 C. The open circuit voltage (OCV) of $Fe_2(MoO_4)_3$/RGO nanocomposite/ Na cells is 2.72 V. The discharge capacities of $Fe_2(MoO_4)_3$/RGO nanocomposite at 0.1 and 0.5 C are about 90.6 mAh g^{-1} and 89.2 mAh g^{-1}, respectively, corresponding to about 20 Na^+ per formula unit (p.f.u), which means completely transformed the Fe^{3+} to Fe^{2+}. It is reason that increases specific capacity of the $Fe_2(MoO_4)_3$/RGO.

The electrochemical performances of $Fe_2(MoO_4)_3$ and the $Fe_2(MoO_4)_3$/RGO nanocomposite in sodium half cell are compares in Figure 4(c). The gravimetric cap cities of $Fe_2(MoO_4)_3$/RGO nanocomposite is calculated based on total weight of the composite that contains about 10 wt.% RGO. The 0.1 C discharge-charge voltage profiles shows at potential plateau at about 2.72 V, which indicates a two phase reaction corresponding to the redox couple of $Fe^{3+/2+}$ and are agreement with the previous experimental results [18]. The initial coulombic efficiency of $Fe_2(MoO_4)_3$/RGO is around 99.6 % and $Fe_2(MoO_4)_3$ powder is about 88.79 %, a relatively low value may be attributed to the kinetic barriers by structural changes during sodium ion extraction/insertion. Trends in the structure $Fe_2(MoO_4)_3$-NASICON has not been fully explained yet, but optimization of the sodium ion cells with electrolyte suitable system can alleviate this issue [9, 27, 39]. Although both samples have similar crystal and the Fe2 (Moo4) 3 phase, but the high rate performance for two samples is quite different. $Fe_2(MoO_4)_3$/RGO nanocomposite provides discharge capacities of 90.60, 89.77, 87.62, and 80.02 mAh g^{-1} at 0.1, 0.5, 1 and 1.5 C, respectively, whereas $Fe_2(MoO_4)_3$ powder delivers the discharge capacities of 80.10 mAh g^{-1} at 0.1 C (Figure 4(c)). It is apparent that the voltage polarization of the composite between the discharge and charge curves are appreciably lower than that of $Fe_2(MoO_4)_3$ powder even at a low capacity rate. The $Fe_2(MoO_4)_3$/RGO nanocomposite exhibits superior capacity maintained a rate of high capacity compared with $Fe_2(MoO_4)_3$ powder as shown in Figure 4 (c). It should be noted that the initial capacity of $Fe_2(MoO_4)_3$/RGO nanocomposite is slowly decrease, although it is discharged at high rate. It can be speculated that the graphene sheets are capable embedded support in an electronic conducting path for composite; therefore, the RGO may be effective in enhancing the electronic conductivity of $Fe_2(MoO_4)_3$. Apparently, the $Fe_2(MoO_4)_3$/RGO nanocomposite shows a larger capacities and better stable cycle than the $Fe_2(MoO_4)$ powder electrode. Specially, at high rates (1.5 C), it is still able to deliver stable capacity of 80.02 mAh g^{-1} that is mantai 93.8 % of theoretical capacity.

The improved specific capacity and discharge at high currents of the $Fe_2(MoO_4)_3$/RGO sample may be related to its nanostructure, which may facilitate the diffusion process. With the increasing of their surface areas, increased contact between electrode and electrolyte, which makes the short path length for both sodium ion diffusion and electronic transport as well as the enhanced ionic and electronic conductivity [18, 28]. The increasing of the current rate, especially at high current, the discharge voltages reduce and the charge voltages increase due to the effect of increasing electrochemical polarization.The $Fe_2(MoO_4)_3$/RGO nanocomposites are short path sodium insertion and holding adsorption of electrolyte wich can reduce electrode polarization when high rate sodium ions insert/extraction. This is further studied by electrochemical impedance spectroscopy method.

Figure 4(d) show the Nyquist plots of $Fe_2(MoO_4)_3$ and $Fe_2(MoO_4)_3$/RGO nanocomposites cathode after 3 cycle at 9 mA g^{-1} in the frenquencies range between 100 kHz and 0.1 Hz at open circuit voltage (OCV) with 5 mV amplitude voltage. The semicircles at high to medium frenquencies is mainly related to a complex reactions process at the cathodic interface/electrolyte. The sloping line in the lower frenquencies region are attributed to the Warburg impedance, that are associated with sodium-ions diffusion in the $Fe_2(MoO_4)_3$ electrode. It can be observed that diameters of high frienquency combined semicircle of $Fe_2(MoO_4)_3$/RGO nanocomposite is smaller than $Fe_2(MoO_4)_3$ powder. The impedance spectrum fitted using an equivalent circuit in which R_e represent the total

resistances of electrolyte, electrodes and separator; R_f and CPE1 are related to the diffusion resistances of Na^+ ions through the solid electrolyte interface (SEI) layers and corresponding constant phase elements (CPE); R_{ct} and CPE2 correspond to charge transfer resistances and the correspond CPE; Z_w is Warburg impedance [22]. The exchange current density is calculated using the following equation:

$$i^o = RT/nFRct \quad (7)$$

The fitting results of R_e, R_f, R_{ct} and i^o as shown in Table 2 indicate that the R_f and R_{ct} values of $Fe_2(MoO_4)_3$/RGO nanocomposite cathode are smaller than that of $Fe_2(MoO_4)_3$ powder. It can be confirmed that the decrease of charge transfer resistances are beneficial to the kinetic behaviors during charge/discharge process. Since the $Fe_2(MoO_4)_3$/RGO nanocomposite shows the lowest resistances and the largest exchange current densities, it is suggested that RGO addition to the $Fe_2(MoO_4)_3$ particle surface significantly improved performances of the sodium-ion batteries.

Table 2. Impedances parameters calculated from equivalent circuit.

Sample	R_e (Ω)	R_f (Ω)	R_{ct} (Ω)	i^o (mA cm^{-2})
$Fe_2(MoO_4)_3$ powder	10.55	120.86	265.60	$4.831x10^{-5}$
$Fe_2(MoO_4)_3$/RGO nanocomposite	6.45	48.26	90.96	$1.411x10^{-4}$

4. CONCLUSIONS

$Fe_2(MoO_4)_3$/RGO nanocomposite was prepared by wet chemistry route, which is the nanostructure formed by $Fe_2(MoO_4)_3$ particles and RGO nanosheets. The porous structures including large specific surfaces and short sodium ion diffusion paths of $Fe_2(MoO_4)_3$/RGO nanocomposite and high conductivity RGO could lead to the good electrochemical properties, especially exhibit perfect cyclability and stalbe structure at high rate when they are used as cathode materials for SIBs. Addition of RGO onto the surface of $Fe_2(MoO_4)_3$ particles significantly improve conductivity and specific surface area, which causes the improvement in the performance of the sodium-ion battery. As the charge/discharge at 1.5 C, the initial specific capacity of $Fe_2(MoO_4)_3$/RGO nanocomposite is 80.02 mAh g^{-1} and remains 75.92 mAh g^{-1} after 50 cycles.

ACKNOWLEDGEMENTS
This work is supported by the International S&T Cooperation program of China (ISTCP) (No. 2013DFR50710), Equipment pre-research project (No. 625010402), Science and Technology Support Program of Hubei Province (No. 2014BAA096), and the National Nature Science Foundation of Hubei Province (No. 2014CFB165).

References

1. B. L. Ellis and N. F. Linda, *Solid State and Materials Science*, 16 (2012) 168
2. M. D. Slater, D. H. Kim, E. Lee and C. S. Johnson, *Adv. Funct. Mater.*, 23 (2013) 947
3. M. Saiful Islam and A. J. Fisher Craig, *Chem. Soc. Rev.*, 43 (2014) 185

4. G. Pistoia, *Lithium batteries*, Elselver, Tokyo (1994) 239-279
5. K. R. Alok, T. A. Ly, G. Jihyeon, M. Vinod and J. Kim, *Ceram. Int.*, 40 (1) (2014) 2411
6. M. M. Doeff, Y. M. Peng, Y. P. Ma and L. D. Jonghe, *J. Electrochem. Soc.*,141 (1994) L145
7. J. Molenda, C. Delmas and P. Hagenmuller, *Solid State Ionics*, 9-10 (1983) 43
8. K. Trad and D. Carlier, *J. Phys. Chem. C*, 114 (2010) 10034
9. Z. L. Jian, L. Zhao, H. L. Pan, S. Y. Hu, H. Li, W. Chen and Q. L. Chen, *Electrochem. Commun.*, 14 (2012) 86
10. J. Kang, S. Baek, M. Vinod, G. Jihyeon, J. Song, Park H, E. Cha, R. A. Kumar and J. Kim, *J. Mater. Chem. A*, 22 (2012) 20857.
11. W. X. Song, X. B. Ji, Y. P. Yao, H. J. Zhu, Q. Y. Chen, Q. Q. Sun and C. E. Banks, *Phys. Chem. Chem. Phys.*,16 (2014) 3055
12. Y. Zheng, P. Zhang, S. Q. Wu, Y. H. Wen, Z. Z. Zhu and Y. Yang, *J. Electrochem. Soc.*, 160 (2013) A927
13. M. W. Xu, L. Wang, X. Zhao, J. Song, H. Xie, H. Y. Lu and J. B. Goodenough, *Phys. Chem.Chem. Phys.*, 15 (2013) 13032
14. K. Chihara, A. Kitajou, I. D. Gocheva, S. Okada and J. Yamaki, *J. Power Sources*, 227 (2013) 80
15. S. M. Oh, S. T. Min, J. Hassoun, B. Scrosati and Y. K. Sun, *Electrochem. Commun.*, 22 (2012) 149
16. A. Sun , F. R. Beck, D. Haynese, J. A. Poston, S. R. Narayanan, P. N. Kumta and A. Manivannan, *Materials Science and Engineering* B, 177 (2012) 1729
17. D. W. Su and G. X. Wang, *ACS Nano*, 7 (12) (2013) 11218
18. Q. Sun, Q. Q. Ren and Z. W. Fu, *Electrochem. Commun.*, 23 (2012) 145
19. W. X. Song, X. B. Ji, Z. P. Wu, Y. C. Yang, Z. Zhou, F. Q. Li, Q. Y. Chen and C. E. Banks, *J. Power Sources*, 256 (2014) 258
20. M. J. Aragón, C. Vidal-Abarca, P. Lavela and J. L.Tirado, *J. Power Sources*, 252 (2014) 208
21. J. Liu, K. Tang, K. P. Song, A. A. Peter, Y. Yu, and J. C. Maier, *Nanoscale*, 6 (2014) 5081
22. V. T. Nguyen, Y. L. Liu, X. Yang and W. Chen, *ECS Electrochem. Lett.*, 4(3) (2015) A29
23. C. Luo, Y. J. Zhu, Y. H. Xu, Y. H. Liu, T. Gao, J. Wang and C. S. Wang, *J. Power Sources*, 250 (2014) 372
24. S. C. Han, E. G. Bae, Lim and M. H. Pyo, *J. Power Sources*, 254 (2014) 73
25. K. S. Nanjundaswamy, A. K. Padhi, J. B. Goodenough, S. Okada, H. Ohtsukab, H. Araib and J. Yamakib, *Solid State Ionics*, 92 (1996) l
26. J. Shirakawa M. Nakaya, M. Wakihar and Y. Uchimoto, *J. Phys. Chem. B*, 11 (2007) 1424
27. P. G. Bruce and G. Miln, *J. Solid State Chem.*, 89 (1989) 162
28. L. L. Liu and Y. H. Xu, *Nano Lett.*, 12 (2012) 5664
29. M. Zhi, C. Xiang, J. Li, M. Li and N. Wu, *Nanoscale*, 5 (2013) 72
30. W. Shen, C. Wang, H. M. Liu and W. S. Yang, *Chemistry - A European Journal*, 19 (43) (2013) 14712
31. W. J. Hao and H. H. Zhan, J. Yu, *Mater. Lett.*, 83 (2012) 121
32. Y. Jiang, W. W. Xu, D. D. Chen, Z. Jiao, H. J. Zhang, Q. L. Ma, X. H. Cai, B. Zhao and Y. L. Chu, *Electrochim. Acta*, 85 (2012) 377
33. Z. S. Wu, G. M. Zhou, L. C. Yin, W. C. Ren, F. Li and H. M. Cheng, *Nano Energy*, 1 (2012) 107
34. Z. L. Hou, W. L. Song, P. Wang, M. J. Meziani, C. Y Kong, A. Anderson, H. Maimaiti, G. E. LeCroy, H. J. Qian and Y. P. Sun, ACS Appl. Mater. Interfaces, 6 (17) (2014) 15026
35. S. L. Candelaria, Y. Y. Shao, W. Zhou, X. L. Li, J. Xiao, J. G. Zhang, Y. Wang, J. Liu, J. H. Li and G. Z. Cao, *Nano Energy*, 1 (2012) 195
36. A. Chavez-Valdez, M. S. P. Shaffer and A. R. Boccaccini, J. Phys. Chem. B, 117 (6) (2013) 1502.
37. M. Pumera, *Energy Environ. Sci.*, 4 (2011) 668
38. Y. H. Jung, C. H. Lim and D. K. Kim, *J. Mater. Chem. A*, 1 (2013) 11350.
39. C. J. Zhao, S. L. Chou, Y. X. Wang, C. F. Zhou, H. K. Liu and S. X. Dou, *RSC Adv.*, 3 (2013) 16597